Journal of
Materials Chemistry A

Boosting the performance of reversible solid oxide electrochemical cells with a novel hybrid oxygen electrode, $Pr_{1.39}Ba_{0.14}Sr_{0.53}Co_{1.48}Fe_{0.76}O_{6-��}$-$Ba_{0.66}Sr_{0.34}CoO_{3-��}$

Journal:	*Journal of Materials Chemistry A*
Manuscript ID	TA-ART-06-2023-003629.R1
Article Type:	Paper
Date Submitted by the Author:	02-Sep-2023
Complete List of Authors:	Fang, Liyang; Kansas State University, Liu, Fan; Kansas State University, Department of Chemical Engineering; Kansas State University Diercks, D.; Colorado School of Mines, Metallurgical and Materials Engineering Kumar, Praveen; Colorado School of Mines, Metallurgical and Materials Engineering Zhao, Feng; Storagenergy Technologies, Inc. Ding, Dong; Idaho National Laboratory, Energy & Environment Science and Technology Duan, Chuancheng; Kansas State University, Chemical Engineering

Boosting the performance of reversible solid oxide electrochemical cells with a novel hybrid oxygen electrode, $Pr_{1.39}Ba_{0.14}Sr_{0.53}Co_{1.48}Fe_{0.76}O_{6-\delta}$-$Ba_{0.66}Sr_{0.34}CoO_{3-\delta}$

Authors: Liyang Fang[1], Fan Liu[1], David Diercks[2], Praveen Kumar[2], Feng Zhao[3], Dong Ding[4, *], Chuancheng Duan[1, *]

Affiliations:

1. Department of Chemical Engineering, Kansas State University, Manhattan, KS, United States
2. Shared Instrumentation Facility, Colorado School of Mines, Golden, CO, United States
3. Storagenergy Technologies Inc., Salt Lake City, UT, United States
4. Energy and Environmental Science and Technology, Idaho National Laboratory, Idaho Falls, ID 83415, USA

Corresponding author: DD: dong.ding@inl.gov, CD: cduan@ksu.edu

Abstract

Solid oxide electrochemical cells (SOECs) stand out as a highly promising clean energy technology that offers several benefits, showing significant potential to play a pivotal role in the transition towards a sustainable and low-carbon energy future. SOECs can efficiently convert the chemical energy stored in fuels to electricity in fuel cell mode, and produce various chemicals from abundant feedstocks (e.g., CO_2, H_2O) and intermittent solar/wind-based renewable electricity. Despite extensive efforts that have been devoted to designing novel materials and optimizing SOEC manufacturing processes, aiming to achieve enhanced energy efficiency, the current SOECs still suffer from poor performance, which is mainly due to the sluggish oxygen reduction reaction (ORR) and oxygen evolution reaction (OER) kinetics. To address this challenge, in this work, we have successfully designed an in-situ formed hybrid oxygen electrode material ($Pr_{1.39}Ba_{0.14}Sr_{0.53}Co_{1.48}Fe_{0.76}O_{6-\delta}$-$Ba_{0.66}Sr_{0.34}CoO_{3-\delta}$), which significantly improves the surface oxygen exchange coefficient and bulk oxygen-ion diffusion coefficient, enhancing the OER and ORR electrocatalytic activities. The SOECs equipped with this newly developed oxygen electrode achieved exceptional performance for power generation using both hydrogen and propane as the fuels. At 750 °C, a peak power density of 2.4 W cm^{-2} was obtained with H_2 as the fuel. Additionally, the SOECs attain unprecedented performance in steam electrolysis mode. A current density of 4.4 A cm^{-2} was achieved at 1.3 V and 750 °C, which represents the highest performance among all yttria-stabilized zirconia (YSZ) electrolyte-based SOECs. The SOECs also deliver remarkable stability during the accelerated stability testing, highlighting the great potential of $Pr_{1.39}Ba_{0.14}Sr_{0.53}Co_{1.48}Fe_{0.76}O_{6-\delta}$-$Ba_{0.66}Sr_{0.34}CoO_{3-\delta}$ as a high-performance oxygen electrode for next generation SOECs.

Introduction

The growing concern over global greenhouse effects and climate change has led to a surge in demands for clean and sustainable energy across the globe. This has generated significant interest in highly efficient energy technologies that produce considerably less greenhouse gas emissions [1]. Among such technologies, SOECs have emerged as a promising option for next-generation electrochemical energy conversion and storage systems, due to their exceptional efficiency and minimal environmental impact. In fuel cell mode, SOECs convert fuels such as hydrogen and hydrocarbons into electricity with a higher efficiency than combustors [2]. When there is excess electricity available, SOECs function as electrolyzers to produce hydrogen, carbon monoxide or syngas with different reactants fed to the fuel electrode [3–7]. SOEC technology has undergone drastic improvements over the past decade, but for its commercialization, further research and development are needed to increase the performance (i.e., energy efficiency and durability) at reduced operating temperatures. However, the notoriously sluggish oxygen reduction reaction (ORR) and oxygen evolution reaction (OER) that occur at the oxygen electrode inevitably have increased the area-specific electrode polarization resistance (ASR_P) with lower operating temperatures, which is ascribed to their thermally activated nature. Therefore, extensive efforts have been invested in developing oxygen electrode materials to alleviate the restricted electrochemical activity and decreased performance [8–14].

Recently, the application of double perovskite-based oxygen electrodes, for example, $PrBa_{0.5}Sr_{0.5}Co_{1.5}Fe_{0.5}O_{6-\delta}$ (PBSCF-a) to fuel electrode-supported YSZ-based SOECs, has attracted a great deal of attention due to their enhanced ORR and OER activity and improved durability. Li et al. have demonstrated an in-situ assembly process for fabricating oxygen electrodes, which leads to the PBSCF-GDC composite oxygen electrode, achieving a peak power density (PPD) of 1.37 W cm^{-2} in fuel cell mode at 750 °C [15]. Tian et al. have employed PBSCF-a as the SOEC oxygen electrode, which achieved an electrolysis current density of 1.74 A cm^{-2} at 2.0 V at 800 °C [16]. Zhang et al. have also reported an oxygen electrode with a PBSCF-infiltrated YSZ scaffold structure, attaining a low ASR_P of 0.03 Ω cm^2 and stable electrolysis performance at 700 °C for 600 h [8]. However, to fabricate effective nanostructured oxygen electrodes, several repeated infiltration/annealing cycles in the wet infiltration process are required, which limits its scale-up and commercial applications. Other novel oxygen electrode processing methods, such as freeze-casting [17], atomic layer deposition [18], and electrostatic spray deposition [19] are also limited by high fabrication cost, complex procedures, and low scalability issues.

More efforts should be, therefore, devoted to developing highly active oxygen electrodes via efficient and facile fabrication methods. To achieve this goal, Chen et al. have developed a nanostructured composite oxygen electrode, which is composed of $PrBa_{0.8}Ca_{0.2}Co_2O_{5+\delta}$ (PBCC) that is decorated with $Gd_{0.2}Ce_{0.8}O_{1.9}$ (GDC), via an in-situ assembly approach [20]. The resulting SOECs achieve a PPD of 1.74 W cm^{-2} in fuel cell mode at 750 °C and an electrolysis current density of 1.77 A cm^{-2} at 1.3 V. With employing a similar oxygen electrode processing method, Liu et al. have designed an $Er_{0.4}Bi_{1.6}O_{3-\delta}$ (ESB) functionalized $La_{0.8}Sr_{0.2}MnO_{3-\delta}$ (LSM) oxygen electrode, which leads to improved performance in both fuel cell and electrolysis modes [21].. Despite the outstanding progress that has been achieved with developing and employing novel oxygen electrode materials, the power density in fuel cell mode and energy efficiency in electrolysis mode can be further enhanced to boost the benefits of SOECs.

Herein, we report a hybrid oxygen electrode that is composed of $Pr_{1.39}Ba_{0.14}Sr_{0.53}Co_{1.48}Fe_{0.76}O_{6-\delta}$ (PBSCF-b) and $Ba_{0.66}Sr_{0.34}CoO_{3-\delta}$ (BSC), which was fabricated via the in-situ formation process. This newly developed hybrid oxygen electrode material was first employed as the oxygen electrode for oxygen-ion conducting SOECs, which leads to improved performance in both fuel cell and electrolysis modes. Extensive characterization was performed to better understand how the BSC phase synergizes with the PBSCF-b phase to enhance OER and ORR performance. We have identified that this composite electrode simultaneously improves the surface oxygen exchange and bulk oxygen-ion diffusion coefficients. The resulting SOECs obtained exceptional performance for power generation using both hydrogen and propane as the fuels. At 750 °C, an exceptional peak power density of 2.4 W cm^{-2} was achieved. Additionally, the SOECs attain unprecedented performance in steam electrolysis mode. A current density of 4.4 A cm^{-2} was achieved at 1.3 V and 750 °C, which represents the highest performance among all Yttria-stabilized zirconia (YSZ) electrolyte-based SOECs (Table S1) [4,6,22–31]. The SOECs also deliver remarkable stability during the accelerated stability testing, highlighting the great potential of $Pr_{1.39}Ba_{0.14}Sr_{0.53}Co_{1.48}Fe_{0.76}O_{6-\delta}$-$Ba_{0.66}Sr_{0.34}CoO_{3-\delta}$ as a high-performance oxygen electrode for next generation SOECs.

Experimental

Material synthesis

$Pr_{1.39}Ba_{0.14}Sr_{0.53}Co_{1.48}Fe_{0.76}O_{6-\delta}$-$Ba_{0.66}Sr_{0.34}CoO_{3-\delta}$ (PBSCF-b+BSC) electrode material

The PBSCF-b+BSC oxygen electrode material was synthesized using the wet-chemistry method, in which high-purity precursors, $Ba(NO_3)_2$, $Sr(NO_3)_2$, $Co(NO_3)\bullet 6H_2O$, and $Fe(NO_3)_3\bullet 6H_2O$ (Fisher Scientific) were dissolved in deionized water in stoichiometric amounts. Additionally, a specific amount of Pr_6O_{11} (Fisher Scientific) was dissolved in diluted nitric acid and subsequently added into the above solution. Then the complexing and chelating agents, ethylenediaminetetraacetic acid (EDTA) (Fisher Scientific) and citric acid (CA) (Fisher Scientific) were added to above solution in appropriate amounts, with a molar ratio of 2:2:1 (EDTA: CA: total metal ions). After continuous stirring for one hour at room temperature, ammonium hydroxide solution was added into the solution to adjust the pH to ~9. The resulting solution was heated to 300 °C on a hot plate with continuous stirring until a gel was formed. This gel was then dried in an oven at 175 °C overnight, and the resulting black powder was calcined at 650 °C under air for 5 hours, followed by ball-milling in ethanol for 24 hours and drying at 175 °C to obtain the final powder for the oxygen electrode ink. After sintering at 750-770 °C, the calcined powder was crystallized to the PBSCF-b+BSC hybrid electrode material.

Previous $PrBa_{0.5}Sr_{0.5}Co_{1.5}Fe_{0.5}O_{6-\delta}$ (PBSCF-a) electrode material

The previous PBSCF-a electrode powder was also synthesized via the wet-chemistry method described above. However, the powder obtained after calcination at 650 °C was later sintered at 900 °C and crystallized to the previous PBSCF-a.

Electrical conductivity relaxation (ECR) samples

The synthesis processes for ECR materials, namely, $Pr_{1.39}Ba_{0.14}Sr_{0.53}Co_{1.48}Fe_{0.76}O_{6-\delta}$, $Ba_{0.66}Sr_{0.34}CoO_{3-\delta}$, and previous $PrBa_{0.5}Sr_{0.5}Co_{1.5}Fe_{0.5}O_{6-\delta}$ were the same as the above wet-chemistry method. Briefly, stoichiometric amounts of $Ba(NO_3)_2$, $Sr(NO_3)_2$, and $Co(NO_3)\bullet 6H_2O$ were used as precursors for BSC powder synthesis. The hybrid electrode, PBSCF-b+BSC is formed at 750-770 °C, while the preparation of a dense PBSCF-b+BSC bar requires a sintering temperature higher than 900 °C. Therefore, a PBSCF-b dense bar was fabricated and then coated with BSC slurry.

Material slurry preparation

Oxygen electrodes slurries

10 g of PBSCF-b+BSC or previous PBSCF-a powder, 2 g dispersant (20 wt.% solsperse 28000 (Lubrizol) dissolved in α-terpinol), and 1 g binder (5 wt.% V-006 (Heraeus) dissolved in α-terpinol) were mixed and ground by mortar and pestle for 0.5 h to obtain the oxygen electrodes slurries.

BSC slurry for ECR testing

Similarly, appropriate amounts of BSC powder were mixed with dispersant and binder, then ground well by mortar and pestle for preparation of the BSC slurry.

Fuel electrode slurry

The composite powder, which consisted of 40 wt.% yttria-stabilized zirconia (YSZ) (TZ-8Y, Tosoh), 60 wt.% NiO (Sigma Aldrich), and 20 wt.% corn starch (Sigma Aldrich), was mixed with menhaden fish oil, b-98 polyvinyl butyral, polyethylene glycol 400, cyclohexanone, di-n-butyl phthalate, xylenes, and ethanol, and then ball-milled using YSZ beads (diameter = 10 mm) for 24 h to obtain the fuel electrode slurry.

Electrolyte slurry

Similarly, the electrolyte slurry was also prepared by mixing and ball-milling YSZ powder and the above organic materials and ethanol.

SOEC cell manufacturing and testing

SOEC half-cell manufacturing

The fuel electrode-supported half-cells of YSZ-NiO were fabricated through a tape-casting process. The prepared fuel electrode slurry was first coated on Mylar via tape-casting and then dried in air for 5 h. The single-layer fuel electrode serves as both a functional layer and a support layer. The electrolyte slurry was then cast on the fuel electrode support layer. The resulting two layers were dried in air for 24 h, followed by sintering at 1350 °C for 5 h to fabricate the SOEC half-cells.

SOEC single cell testing with PBSCF-b+BSC oxygen electrode

The hybrid oxygen electrode slurry was first brush-painted on the YSZ electrolyte surface and then dried at 180 °C on a hot plate for 0.5 h. Gold paste was applied on both electrodes and so was a silver grid for current collection. The obtained single cells were directly sealed on an alumina tube with the MO·SCI glass sealant (OL-GL1709P/-45) without pre-sintering the oxygen electrode. The testing station temperature was increased to 765 °C with a heating rate of 4 °C/min, to melt the sealing glass while the PBSCF-b+BSC hybrid electrode was obtained simultaneously. Then the SOEC single cell was tested at temperatures ranging from 750 °C to 550 °C. Ambient air (300 sccm) and humidified hydrogen (or propane) with a flow rate of 50 sccm, were fed to the oxygen and fuel electrodes, respectively. To evaluate the fuel cell performance, the hydrogen was flowed through a bubbler at room temperature, while for electrolysis evaluation, a boiler was used instead, to obtain a hydrogen flow with 40% humidity.

Prior to the electrochemical characterization, a mixture of H_2 and Ar gas flow (20 sccm) was fed to reduce the NiO to Ni at the fuel electrode. The electrochemical impedance spectroscopy (EIS) and I-V curve measurements were performed using Gamry Reference series potentiostat/galvanostat/ZRAs, including 1000, 3000 and 5000. EIS data was collected over a frequency range of 10 kHz – 0.1 Hz under open circuit conditions or applied voltage.

SOEC single cell testing with previous PBSCF-a oxygen electrode

The previous PBSCF-a slurry was brush-painted on the YSZ electrolyte surface and then fired at 900 °C for 2 h to obtain the previous PBSCF-a oxygen electrode. The following single cell testing procedure was the same as mentioned above.

Hydrogen production cost calculation

The hydrogen production cost shown in Figure 1B was calculated according to the following equation:

$$Hydrogen\ production\ cost = \frac{V \times j \times 0.001 \times \$0.04/kW \cdot h}{j/(2 \times F \times 3600 \times M_{H_2})}$$

Where *V* is the voltage applied on the SOEC (V), j is the corresponding current density (A cm^{-2}), $\$0.04/kW \cdot h$ represents the unit electricity cost, *F* is the Faraday constant (96485 s A mol^{-1}), and M_{H_2} is the molecular weight of hydrogen (0.001 kg mol^{-1})

Electrical conductivity relaxation (ECR) measurement

ECR testing was utilized to evaluate the surface exchange kinetics of the hybrid electrode and previous PBSCF-a. The previous PBSCF-a powder was first axially pressed at 100 bar for 2 min using a die (diameter = 2 cm), then sintered at 900 °C for 3 h. The resulting dense pellets were cut by a high-precision diamond saw. PBSCF-b+BSC sample was also prepared in a similar manner. $Pr_{1.39}Ba_{0.14}Sr_{0.53}Co_{1.48}Fe_{0.76}O_{6-\delta}$ dense bars were obtained and BSC slurry was then coated on the surface. ECR measurements of these samples were conducted at temperatures ranging from 700 °C to 600 °C. In each measurement, the initial oxygen concentration was set as 2 vol.% (490 sccm Ar + 10 sccm O_2) and a current of 40 mA was applied. After the voltage reached equilibrium, the oxygen concentration was changed to 20 vol.% (400 sccm Ar + 100 sccm O_2) and the voltage response was recorded each time. The resulting data was analyzed using the NETL ECR analysis tool.

Structural characterization

The crystal structures of the hybrid electrode and previous PBSCF-a were determined by using X-ray diffraction (XRD) (Rigaku MiniFlex diffractometer) with a Cu K-alpha radiation source operated at 15 mA and 30 kV and a scanning rate of 1 degree per minute. The Rietveld refinement was further performed via the GSAS program to probe detailed crystal structural information of the PBSCF-b+BSC material. The morphological and cross-sectional properties of the single cells were characterized by scanning electron microscopy (SEM, Hitachi/S-3400 N). Transmission electron microscopy (S/TEM, FEI Talos F200X, Thermo Fisher Scientific) operated at 200 kV was employed to obtain the morphological, and structural information about the oxygen electrode materials, with EDX detectors were utilized for chemical composition characterization.

Results and discussion

Hybrid oxygen electrode enables improved performance in both fuel cell and electrolysis modes

Hybrid oxygen electrodes have been widely developed to enhance SOEC performance for power generation and hydrogen production [14,32–35]. Despite the outstanding results that have been achieved, the performance, especially the energy efficiency in steam electrolysis mode, should be further enhanced to achieve the U.S. Department of Energy (DOE) renewable hydrogen production cost goal of <\$1 kg^{-1} [36], while increasing the hydrogen production rate per active area. Therefore, we have developed a new hybrid oxygen electrode, PBSCF-b+BSC, via the in-situ formation process, which simplifies the oxygen electrode fabrication process and improves the electrocatalytic activity. Figure 1A schematically displays this hybrid electrode, which is composed of the PBSCF-b phase and a minor BSC phase that is dispersed on the PBSCF-b phase. First, the PBSCF-b phase has an improved bulk oxygen-ion diffusion coefficient. Additionally, the BSC phase exhibits a much higher surface oxygen exchange coefficient. Therefore, this composite electrode leads to synergistic effects, which improve the ORR and OER activity.

As shown in Figures 1B-1D, the YSZ-based SOECs equipped with this new hybrid electrode achieve remarkable performance for both hydrogen production and power generation (Table S2) [3–7,16,20–23,37–40]. First, as displayed in Figure 1B, the SOECs simultaneously attain high hydrogen production rate, while achieving lower hydrogen production cost than SOECs reported in literature (see Materials and Methods). At 750 °C and 1.3 V, our SOECs obtain a current density of 4.4 A cm^{-2}, which represents the highest performance among all YSZ-based SOECs (Figure 1C). Furthermore, our SOECs also realize exceptional fuel cell performance using hydrogen and propane as the fuel (Figure 1D). These promising results have emphasized that PBSCF-b+BSC is a high-performing oxygen electrode for SOECs.

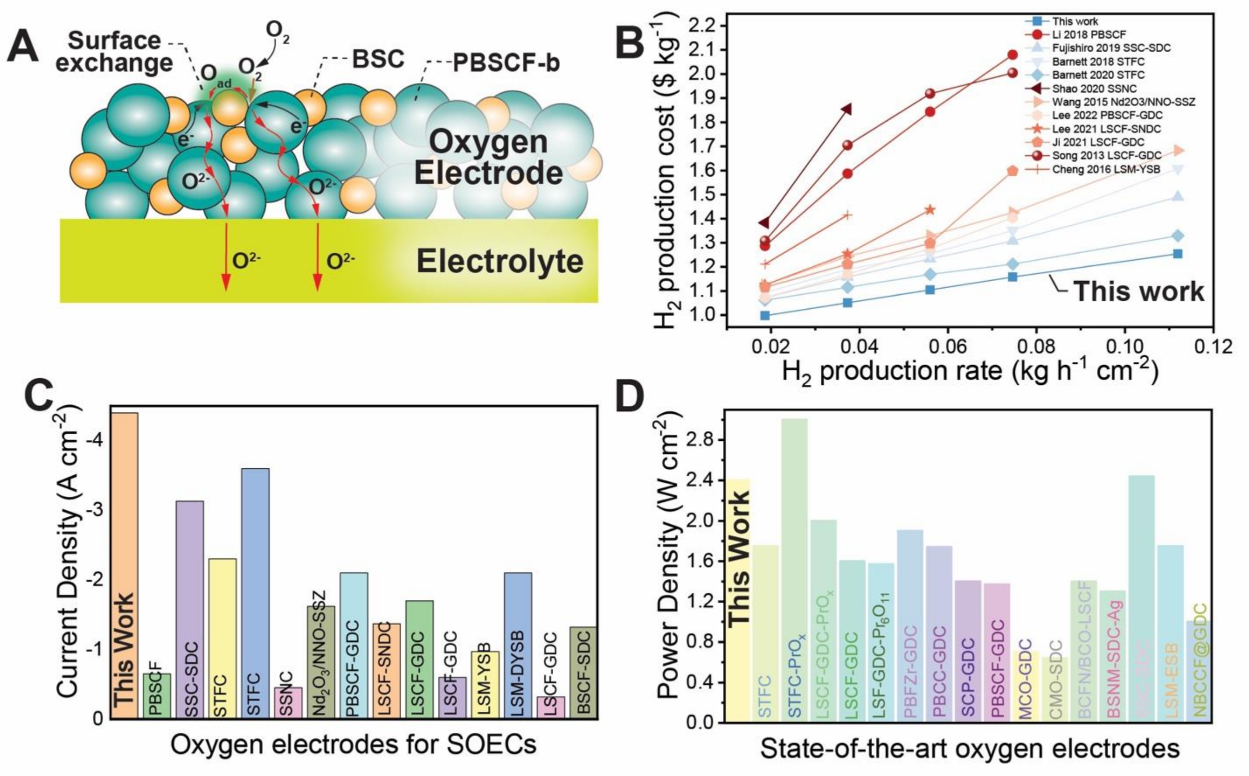

Figure 1. The hybrid oxygen electrode leads to exceptional performance in both fuel cell and electrolysis modes. (A) Schematic illustration of the SOEC with the newly developed hybrid electrode in fuel cell mode, which displays the oxygen reduction reaction. **(B)** The H_2 production cost as a function of H_2 production rate achieved in this work and reported in literature results [4,6,22–31]. **(C)** Performance comparison of YSZ-based SOECs in steam electrolysis mode, which indicates our SOECs equipped with the hybrid oxygen electrode achieve unprecedented performance (Table S1). **(D)** Comparison of peak power densities of our YSZ based SOEC in fuel cell mode with literature results (Table S2).

Structural properties of the in-situ formed hybrid electrode

The hybrid electrode was synthesized via the wet-chemistry method, which has been widely used for synthesizing SOEC electrode materials [24,41–43]. In brief, a stoichiometric amount of the precursors (Pr_6O_{11}, $Ba(NO_3)_2$, $Sr(NO_3)_2$, $Co(NO_3)_2 \cdot 6H_2O$, and $Fe(NO_3)_3 \cdot 9H_2O$) was mixed with DI water, chelating agents (citric acid and ethylenediaminetetraacetic acid), and ammonium hydroxide solution, which was then stirred and heated at 300 °C for 5-10 hours, leading to the production of a gel. The gel was dried at 175 °C overnight and then calcined at 650 °C for 5 h to achieve highly porous black powder, which was subsequently calcined at 750-770 °C to obtain the hybrid electrode. Additionally, we synthesized the previous single-phase PBSCF-a as the baseline material (see Materials and Methods).

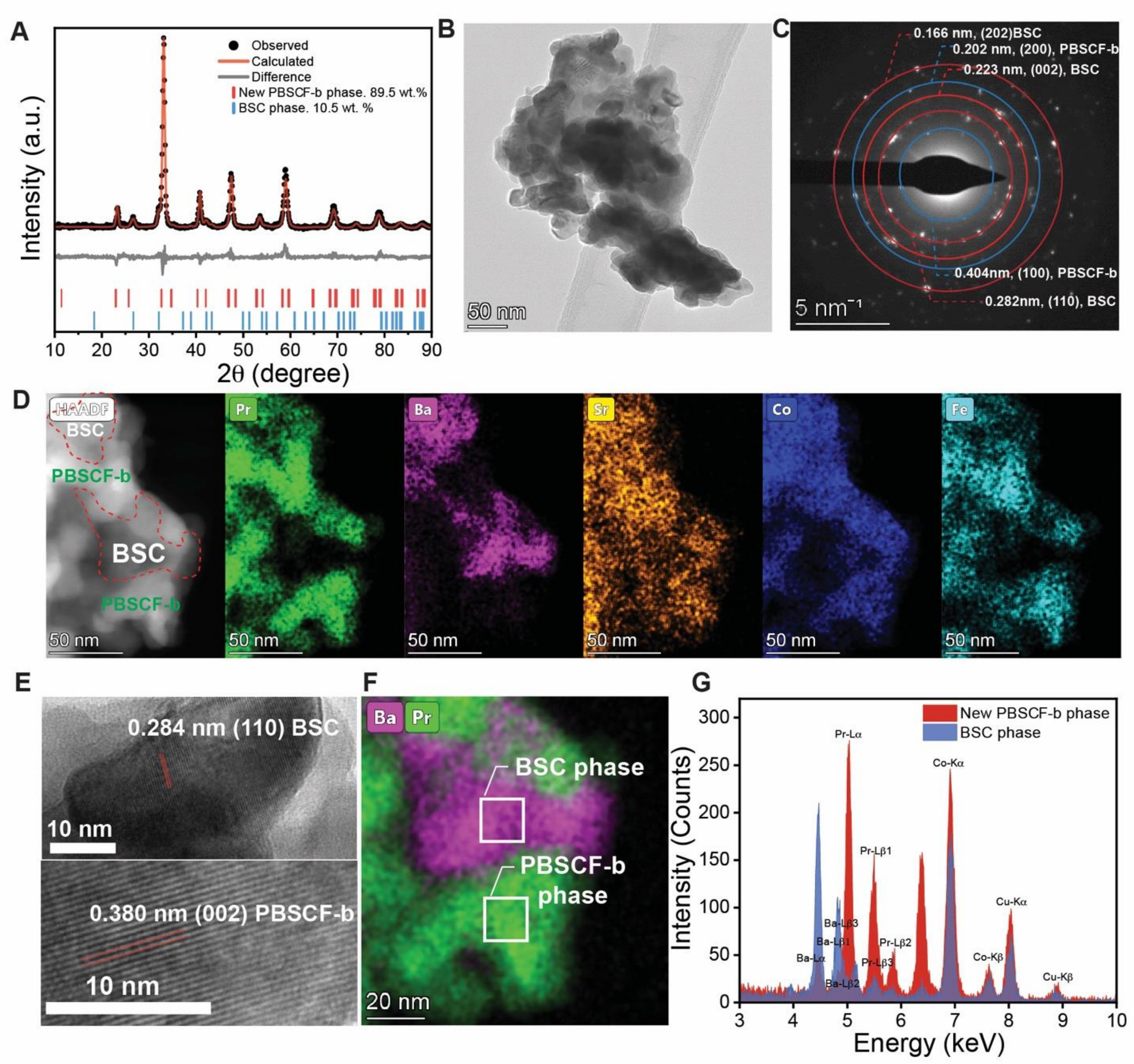

Figure 2. Crystal structure, microstructure, and chemical compositions of the hybrid electrode. (A) the XRD pattern and Rietveld refinement of as-synthesized hybrid electrode. **(B)** Bright-field TEM image of the hybrid electrode. **(C)** The SAED patterns collected from the area shown in (B). **(D)** HAADF-STEM image and corresponding EDX elemental mapping images of

the hybrid electrode**.** **(E)** HR-TEM images of PBSCF-b phase and BSC phase. **(F)** Overlay, chemical mapping image with both Ba and Pr elements, which shows the Ba-rich area (magenta) is BSC and the Pr-rich area (green) is the PBSCF-b phase. **(G)** EDX spectra of the BSC phase and PBSCF-b phase (see the marked boxes in Fig 2F), which were used to quantify the stoichiometries of these two phases.

Figure 2A displays the XRD pattern of the in-situ formed hybrid electrode, which confirms that this new composite electrode is composed of a new PBSCF-b phase (tetragonal, P4/mmm) and a BSC phase (hexagonal, P63/mmc). The following TEM-EDX results were used to quantitively determine the exact stoichiometries for both phases ($Pr_{1.39}Ba_{0.14}Sr_{0.53}Co_{1.48}Fe_{0.76}O_{6-\delta}$ and $Ba_{0.66}Sr_{0.34}CoO_{3-\delta}$), which were used as the input to perform the Rietveld refinement. As shown in Figure 2A and Table S3, it has been identified that the hybrid electrode consists of 89.5 wt. % PBSCF-b phase and 10.5 wt. % BSC phase. Additionally, the refinement achieves a Chi value of 1.978, and both wRp and Rp values remain below 15%, indicating the refinement is reliable and the chemical stoichiometries determined by TEM-EDX are consistent with the refinement results. On the other hand, as shown in Figure S1, the previous PBSCF-a is a single phase (orthorhombic, Pmmm).

Transmission electron microscopy (TEM), energy dispersive X-ray spectroscopy (EDX), and selected area electron diffraction (SAED) were performed to better study the microstructure, crystal structure, and chemical compositions of this new hybrid electrode. The hybrid electrode powder displays a microstructure of nanosized particles with a particle size of ~50 nm (Figure 2B). The SAED patterns as shown in Figure 2C further validate that this hybrid electrode is composed of the BSC phase and a PBSCF-b phase. The diameter of each ring corresponds to the interplanar distance (d-spacing) of crystal planes present in this electrode. The d-spacing values of 0.166 nm, 0.223 nm, and 0.282 nm correspond to (202), (002), and (110) planes of BSC, respectively. The d-spacing values of 0.202 nm, 0.404 nm, and 0.273 nm corresponding to (200), (100), and (102) planes of the PBSCF-b phase (Figure S2). These results are consistent with the high-resolution TEM (HR-TEM) images shown in Figure 2E and the XRD refinement results (Table S3).

Additionally, S/TEM-EDX images and spectra were collected to quantitively determine the stoichiometries of both phases presented in the hybrid electrode. The EDX mapping images shown in Figure 2D clearly show that the hybrid electrode consists of one Ba-rich phase and one Pr-rich phase, which correspond to the BSC and PBSCF-b, respectively. The detailed analysis of the EDX spectrum shown in Figure 2G determines the stoichiometry of the BSC phase as $Ba_{0.66}Sr_{0.34}CoO_{3-\delta}$, while that of the new PBSCF-b phase is $Pr_{1.39}Ba_{0.14}Sr_{0.53}Co_{1.48}Fe_{0.76}O_{6-\delta}$. The presence of both phases is further substantiated by the additional mapping images depicted in Figure S3 and S4. As mentioned above, these stoichiometries were used to perform the XRD refinement with valid results, indicating that the stoichiometries are correct.

Hybrid oxygen electrode enhances surface oxygen exchange coefficient and bulk oxygen-ion diffusion coefficient, leading to improved electrochemical performance

We hypothesized that the two phases in the hybrid electrode can synergize to achieve improved electrochemical properties, such as faster surface oxygen exchange and bulk oxygen-ion diffusion kinetics. Therefore, electrical conductivity relaxation (ECR) was performed, and subsequent analysis using the NETL-developed software [44] was conducted to determine the surface oxygen exchange coefficient (k_{chem}) and bulk oxygen-ion diffusion coefficient (D_{chem}) (Figure S5, S6). Figure 3A compares the k_{chem} of this new hybrid electrode and previous PBSCF-a, indicating that the hybrid electrode significantly accelerates the surface oxygen exchange kinetics. For example, at 700 °C, the k_{chem} of the hybrid electrode is 1.6×10^{-4} cm s^{-1}, which is 45% higher than that of previous PBSCF-a (1.1×10^{-4} cm s^{-1}). Additionally, the corresponding activation energy of the hybrid electrode (87.1 kJ mol^{-1}) is much lower than the previous PBSCF-a (123.9 kJ mol^{-1}), indicating that the surface oxygen exchange process exhibits lower energy barrier, which is essential for achieving high ORR and OER activity at reduced operating temperatures. Furthermore, Figure 3B shows that the D_{chem} of the hybrid electrode is also higher than that of previous PBSCF-a. Moreover, the corresponding activation energy of the hybrid electrode is also lower than that of previous PBSCF-a. These results imply that the hybrid electrode can be employed to build SOECs operating at reduced operating temperatures.

We also measured and compared the area-specific electrode polarization resistance (ASR_p) and ohmic resistance (ASR_{ohm}) of SOECs with the hybrid electrode and the previous PBSCF-a electrode. As shown in Figure 3C, the new hybrid electrode leads to a much lower ASR_p than the previous PBSCF-a electrode, affirming the conclusion that the hybrid electrode can achieve improved electrocatalytic activity. Furthermore, the Arrhenius plots of ASR_p as a function of operating temperature show that the hybrid electrode exhibits a lower activation energy (42.0 kJ mol^{-1}) than that of the previous electrode (44.8 kJ mol^{-1}), which is consistent with the k_{chem} and D_{chem} results. On the other hand, employing the new hybrid electrode does not obviously affect the ASR_{ohm} (Figure 3D), indicating that the hybrid electrode does not lead to any deleterious chemical reactions between the electrode and oxygen electrode, suggesting that the new hybrid electrode is chemically compatible with the electrolyte.

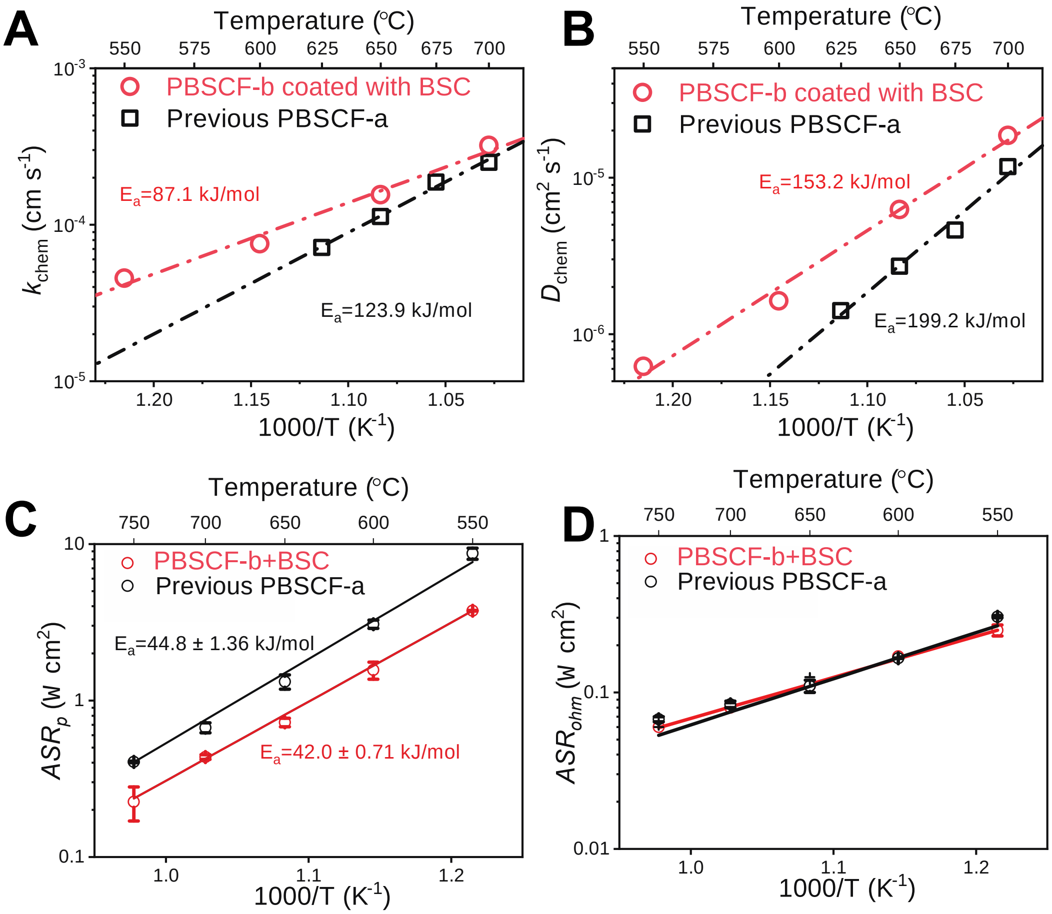

Figure 3. Electrochemical performance comparison of the hybrid electrode with the previous PBSCF-a. **(A)** surface oxygen exchange coefficients (k_{chem}) and **(B)** bulk oxygen-ion

diffusion coefficient (D_{chem}) for the hybrid electrode and previous PBSCF-a. **(C)** Area-specific electrode polarization resistance (ASR_p) of SOECs equipped with the hybrid electrode and the previous PBSCF-a electrode, which were measured under OCV conditions. **(D)** Area-specific ohmic resistance (ASR_{ohm}) of SOECs equipped with the hybrid electrode and the previous PBSCF-a electrode, which were measured under OCV conditions.

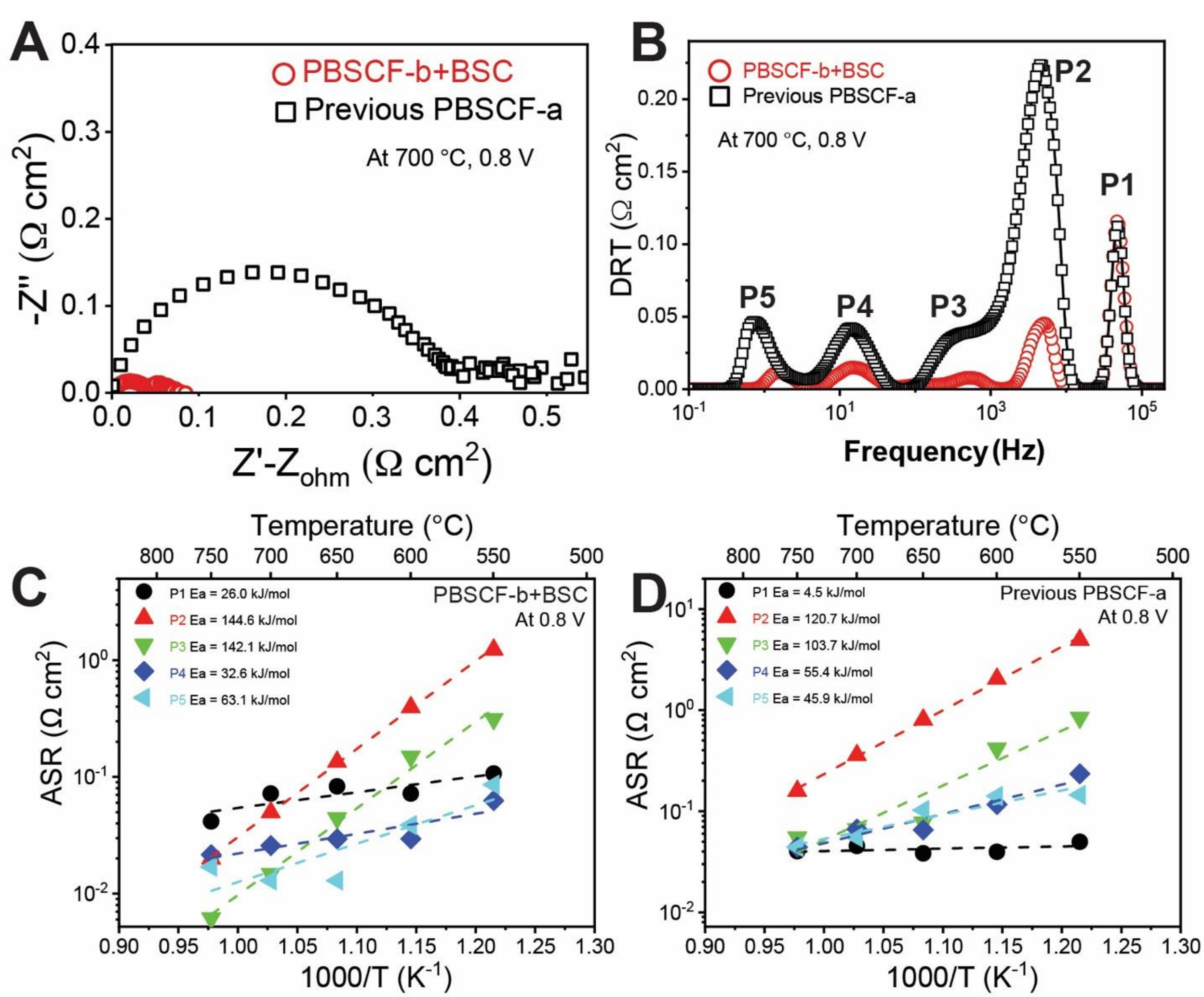

Figure 4. Distribution of relaxation time (DRT) analysis of EIS spectra collected from SOECs equipped with the new hybrid electrode and previous PBSCF-a electrode. (A) Representative EIS comparison at 700 °C under 0.8 V. **(B)** DRT analysis of EIS data shown in (A). **(C)** and **(D)** Temperature dependence of the partial polarization resistances of the electrode reactions of SOFCs with these two electrodes at 0.8 V, respectively.

To gain an in-depth understanding of why the hybrid electrode leads to improved electrochemical performance, the distribution of relaxation time (DRT) analysis of EIS spectra was performed. The DRT analysis is a convenient and potent method for distinguishing the resistance ascribed to different processes occurring at the electrodes. To transform EIS data into the time domain, the DRT software developed by Ciucci et al. was used [45], and a Gaussian distribution was employed. Representative EIS spectra at 700 °C and 0.8 V and corresponding DRT analysis results are presented in Figures 4A and 4B. Each DRT analysis plot consists of five distinct peaks, which are denoted as P1- P5, starting from the high frequency. In general, the processes associated with P4 and P5 correspond to mass transfer processes, including the gas diffusion within the pores of both the oxygen electrode and the fuel electrode, and the transport of ionic/electronic defects within the porous solid electrodes [41,46]. The process associated with P3 is likely to be the hydrogen oxidation reaction occurring at the hydrogen electrode (i.e., fuel electrode) [47,48]. The process represented by P2 is deemed as the key step because the integrated area of each peak represents the resistance of the process, and P2 shows the highest resistance [3,46,49]. This process can be ascribed to the surface oxygen exchange process, including oxygen adsorption, dissociation, and surface transport, which is also the main difference between the hybrid electrode and previous PBSCF-a. The process represented by P1 is widely accepted to be the charge transfer process across the electrode/electrolyte interface [41,50].

As shown in Figure 4B, employing the hybrid oxygen electrode primarily reduces the resistance corresponding to the surface oxygen exchange (P2), which further confirms that the hybrid oxygen electrode can significantly facilitate the surface oxygen exchange. This new electrode does not affect the electrolyte/electrode interfacial charge transfer, which is consistent with the results shown in Figure 3D, where the new electrode does not affect ASR_{ohm}. Figure 4B also indicates that the new hybrid electrode slightly reduces the resistance ascribed to the mass transport which could be due to its relatively high porosity as the hybrid electrode was sintered at a lower temperature than the previous PBSCF-a.

After analyzing the DRT peaks, the temperature dependences of the area-specific resistances of each peak were plotted for both the hybrid electrode and the previous PBSCF-a. The resistance of the P2 process, which is associated with the surface oxygen exchange and oxygen ion diffusion processes, has the highest activation energy for both electrode materials. The process that corresponds to P2 mainly contributes to the polarization resistance at relatively low operating temperatures, and this is particularly evident for the previous PBSCF-a. On the other hand, the resistance of the charge transfer at the interface (P1) has a much weaker temperature dependency, which is in good agreement with literature studies [51,52]. For the hybrid electrode, the P1 process is the major contribution in the higher temperature range. However, due to its much lower activation energy, its influence on the total resistance decreases as the temperature decreases. The temperature dependence of the resistance of the P3 process, which is associated with the hydrogen electrode, is strong for both electrode materials, with an activation energy of 142.05 kJ mol^{-1} for the hybrid electrode and 103.73 kJ mol^{-1} for previous PBSCF-a. Compared to other processes, the resistances associated with P4 and P5 are less significant, as the processes associated with P4 and P5 are related to gas diffusion [53].

SOECs equipped with the hybrid oxygen electrode achieve outstanding fuel cell performance.

To assess the SOEC performance in fuel cell mode, a set of SOECs equipped with both the hybrid oxygen electrode and the previous PBSCF-a electrode were tested. Figure S7 shows the lab-scale SOECs employed to evaluate the oxygen electrodes. The oxygen electrode effective area is 0.5 cm^2. As detailed in the Materials and Methods, the SOECs were manufactured via co-tape casting, producing SOEC half cells that were highly reproducible, highly uniform, and defect-free, and had dense electrolytes with a thickness of ~8 µm (Figure S8), which is essential for fairly investigating different oxygen electrode materials.

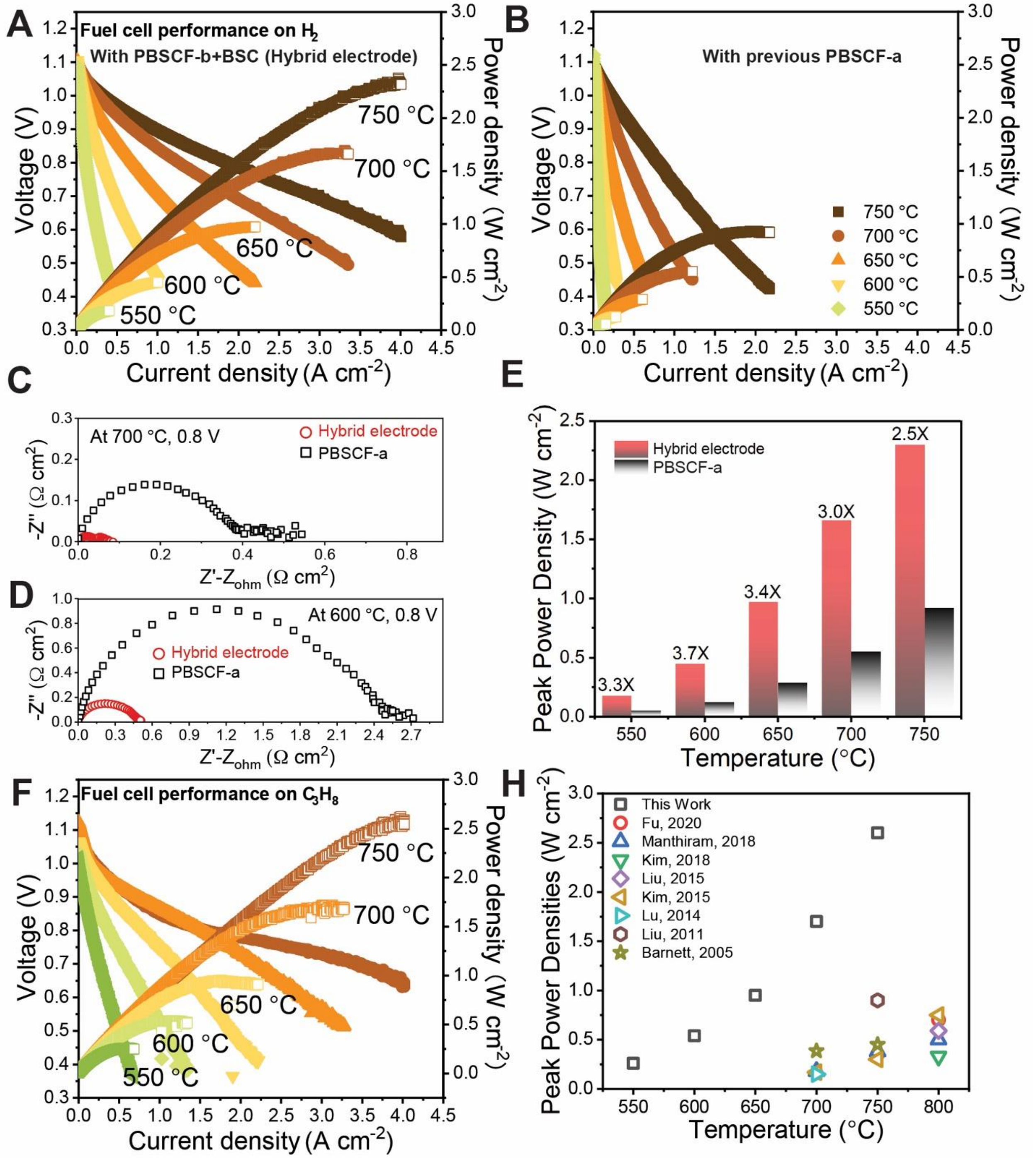

Figure 5. The fuel cell performance of SOECs with the hybrid oxygen electrode. (A) and **(B)** I-V and I-P curves of the SOECs with the hybrid oxygen electrode and previous PBSCF-a electrode at different operating temperatures. H_2 is fed to the fuel electrode as fuel. **(C)** and **(D)** EIS spectra of the SOECs with two electrodes, which were collected at 0.8V, at temperatures of 700 °C and 600 °C. respectively. **(E)** Comparison of the SOEC peak power densities achieved with the hybrid oxygen electrode and previously developed PBSCF-a electrode. **(F)** I-V and I-P curves of the SOEC with the hybrid oxygen electrode. Humidified C_3H_8 was fed to the fuel

electrode as fuel. **(H)** Comparison of our direct-C_3H_8 SOEC with literature results (Table S4) [54–61].

Figure 5 summarizes the fuel cell performance under various conditions. All SOECs tested in this work show an OCV of ~1.1 V at 750 °C, which is close to the theoretical value, indicating that there is no gas leakage and that the performance evaluation is valid. Figure 5A shows that the SOEC with the hybrid oxygen electrode attains peak power densities of 2.4, 1.6, 0.9, 0.4, and 0.2 W cm^{-2} at 750 °C, 700 °C, 650 °C, 600 °C and 550 °C, respectively. The peak power densities achieved with the hybrid electrode are 2-4 times as high as that achieved with the previous PBSCF-a oxygen electrode (Figure 5B-5E). The demonstrated improvement in fuel cell performance can be investigated by conducting EIS, with representative EIS spectra shown in Figures 5C and 5D. Notably, the ASR_p was observed to be much lower using the hybrid oxygen electrode compared to the previous PBSCF-a. Furthermore, the excellent fuel cell performance was also demonstrated using C_3H_8 as the fuel. As shown in Figure 5F, peak power densities of 2.5, 1.6, 0.9, 0.5, and 0.25 W cm^{-2} were demonstrated at 750 °C, 700 °C, 650 °C, 600 °C, and 550 °C, respectively. Figure 5H indicates the direct-C_3H_8 SOECs demonstrated in this work represent the world record performance.

Durability in fuel cell mode at intermediate operating temperatures

The durability of SOECs is crucial for reliable power generation. Li et al. has demonstrated SOECs equipped with PBSCF-a oxygen electrode, which achieves reversible and durable operation at a current density of 0.4 A cm^{-2} for 24 h [62]. In this work, we have conducted short-term stability testing of our SOEC in fuel cell mode with both H_2 and C_3H_8 fed to the fuel electrode. With humidified H_2 fed to the fuel electrode as the fuel, the SOEC achieves durable operation with negligible degradation at a current density of 0.8 A cm^{-2} and temperature of 650 °C. Additionally, the SOEC is durable at 550 °C, which validates the durability of our hybrid oxygen electrode at an intermediate operating temperature. Moreover, we also demonstrated its potential for utilizing alternative fuels (e.g., C_3H_8) for durable power generation, which is shown in Figure 6C. The degradation rates are summarized in Table S7. Overall, the short-term stability testing conducted on SOECs with the hybrid electrode demonstrate its potential for durable power generation using multiple fuel streams.

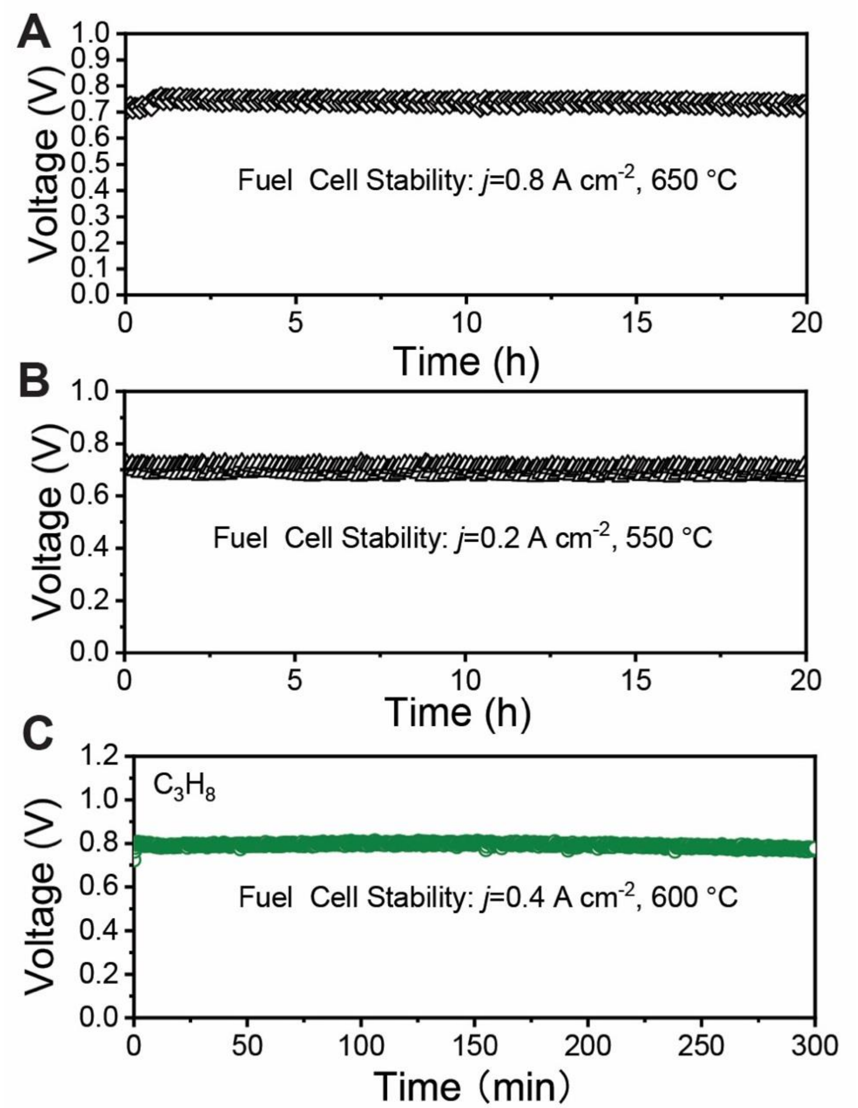

Figure 6. Durability testing of the SOEC equipped with the hybrid oxygen electrode in fuel cell mode. (A) Stability testing at a current density of 0.8 A cm^{-2} and temperature of 650 °C with 3% humidified H_2 fed to the fuel electrode, **(B)** Stability testing at a current density of 0.2 A cm^{-2} and temperature of 550 °C with 3% humidified H_2 fed to the fuel electrode 0.2 A cm^{-2}, and **(C)** Stability testing at a current density of 0.4 A cm^{-2} and temperature of 600 °C with 3% humidified C_3H_8 fed to the fuel electrode.

SOECs equipped with the hybrid oxygen electrode attain a current density of 4.4 A cm^{-2} at 1.3 V and 750 °C, and good durability during the accelerated stability testing

Our SOECs equipped with the hybrid oxygen electrode also attain exceptional performance in steam electrolysis mode. Figure 7A shows the I-V curves of the SOEC in steam electrolysis mode at 550-750 °C. At 750 °C, a current density of 4.4 A cm^{-2} was achieved at 1.3 V, which is higher than the previously reported SOECs (Figure 1C). Additionally, the SOECs demonstrated in this work also result in a cell-level H_2 production cost of 0.997 \$ kg^{-1} at a H_2 production rate of 0.0187 kg h^{-1} cm^{-2}, which represents the state of the art among of YSZ-based SOECs (Figure 1B).

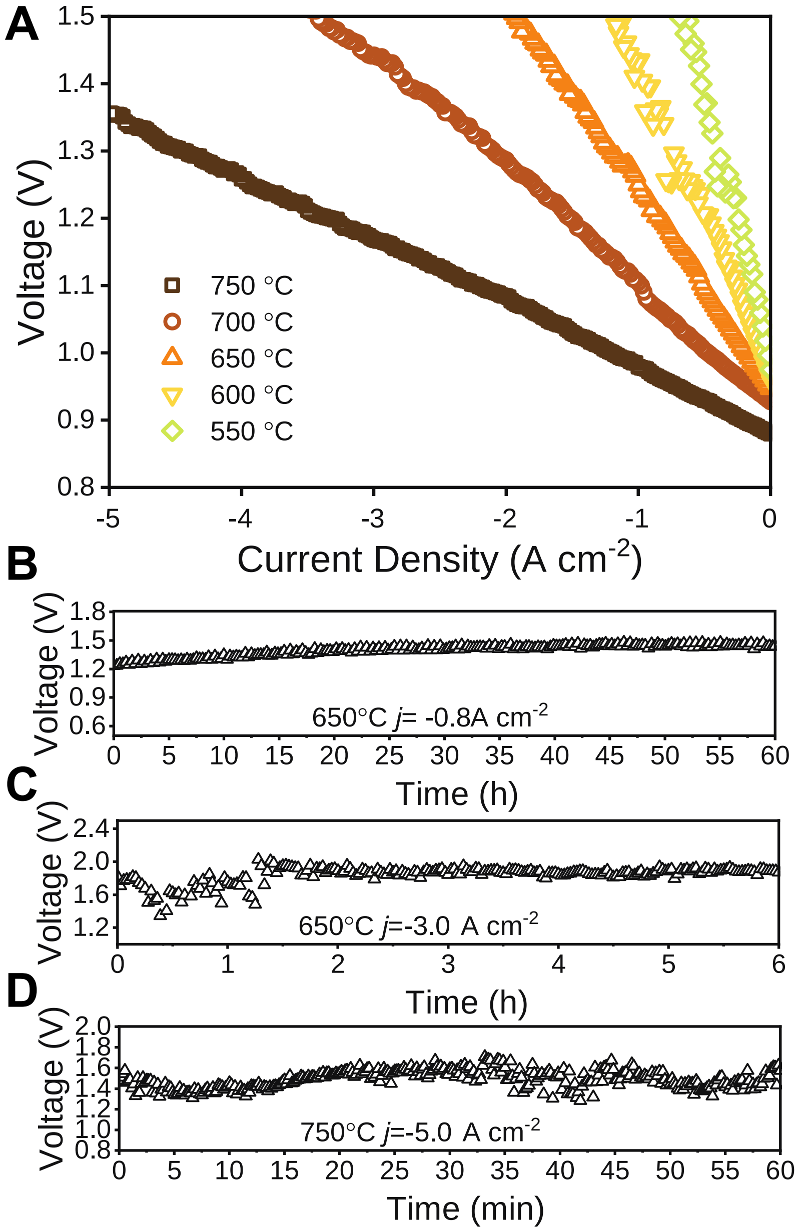

Figure 7. SOEC performance in steam electrolysis mode with 40% steam. (A) *I-V* curves of one representative SOEC with the hybrid oxygen electrode at different operating temperatures. **(B)** Durability testing of the SOEC at a current density of 0.8 A cm^{-2} and temperature of 650 °C. **(C)** Accelerated stability testing of the SOEC in steam electrolysis mode at a high current density of 3.0 A cm^{-2} and temperature of 650 °C**. (D)** Accelerated stability testing of the SOEC in steam electrolysis mode at a high current density of 5.0 A cm^{-2} and temperature of 750 °C**.**

To validate the stability of employing these SOECs for reliable H_2 production, short-term stability was initially tested at 650 °C with a current density of 0.8 A cm^{-2}. The SOEC displays a minor degradation at the early stages and stable operation for the remaining 40 hours. To accelerate the evaluation of SOEC stability, we operated our SOECs under an extremely high current density. For example, as shown in Figure 7C, at 650 °C and a current density of 3.0 A cm^{-2}, the SOEC does not show degradation upon the accelerated stability testing. The second accelerated stability test was performed at 750 °C and a current density of 5.0 A cm^{-2}, which also indicates the SOECs equipped with the new hybrid electrode are stable. The degradation rates are summarized in Table S7, ranging from 3 mV h^{-1} to 4 mV min^{-1}, which are not eligible. Post-mortem characterizations were performed to evaluate the structural stability of SOECs. The SEM images shown in Figure S9 do not show any cracking or electrolyte-electrode delamination, implying the SOEC structure is robust under the harsh testing conditions.

Conclusion

In this work, we have successfully demonstrated a new hybrid oxygen electrode, which is composed of $Pr_{1.39}Ba_{0.14}Sr_{0.53}Co_{1.48}Fe_{0.76}O_{6-\delta}$ and $Ba_{0.66}Sr_{0.34}CoO_{3-\delta}$. This hybrid electrode significantly improves the surface oxygen exchange and bulk oxygen-ion diffusion coefficients, enhancing both oxygen reduction reaction and oxygen evolution reaction kinetics. Extensive characterization and analysis were performed to study this new electrode. The YSZ-based SOECs equipped with this novel hybrid electrode attain unprecedented performance for both power generation in fuel cell mode and green hydrogen production in steam electrolysis mode. At 750 °C, a peak power density of 2.4 W cm^{-2} was achieved using H_2 as the fuel. With propane fed to the fuel electrode, a peak power density of 2.6 W cm^{-2} was attained, representing the record in this field. In steam electrolysis mode, a current density of 4.4 A cm^{-2} was demonstrated at 1.3 V and 750 °C, which outperforms all previously reported YSZ-based SOECs. This achievement leads to a cell-level hydrogen production cost of 0.997 \$ kg^{-1} at a H_2 production rate of 0.0187 kg h^{-1} cm^{-2}, which approaches the DOE H_2 production cost target (<\$1/kg). Additionally, accelerated stability testing was performed in steam electrolysis mode under extremely high current densities (5.0 A cm^{-2}), validating the stability of the SOECs equipped with the newly developed hybrid electrode are stable. These promising results highlight that the PBSCF-b+BSC hybrid electrode could serve as the next-generation oxygen electrode of high-performance SOECs.

Conflicts of interest

There are no conflicts to declare.

Acknowledgements

The Tescan S8252G Raman-SEM/FIB instrument used in this research was purchased with support from the NSF-MRI program (DMR-1828454).

References

1 F. Liu, D. Ding and C. Duan, *Advanced Science*, 2023, **10**, 2206478.

2 F. Liu, D. Diercks, A. M. Hussain, N. Dale, Y. Furuya, Y. Miura, Y. Fukuyama and C. Duan, *ACS Appl. Mater. Interfaces*, 2022, **14**, 53840–53849.

3 Y. Niu, Y. Zhou, W. Lv, Y. Chen, Y. Zhang, W. Zhang, Z. Luo, N. Kane, Y. Ding, L. Soule, Y. Liu, W. He and M. Liu, *Adv. Funct. Mater.*, 2021, **31**, 2100034.

4 S.-L. Zhang, H. Wang, M. Y. Lu, A.-P. Zhang, L. V. Mogni, Q. Liu, C.-X. Li, C.-J. Li and S. A. Barnett, *Energy Environ. Sci.*, 2018, **11**, 1870–1879.

5 B.-K. Park and S. A. Barnett, *J. Mater. Chem. A*, 2020, **8**, 11626–11631.

6 B.-K. Park, R. Scipioni, Q. Zhang, D. Cox, P. W. Voorhees and S. A. Barnett, *J. Mater. Chem. A*, 2020, **8**, 11687–11694.

7 X. Tong, Y. Xu, Đ. Tripković, P. V. Hendriksen, W.-R. Kiebach and M. Chen, *J. Mater. Chem. A*, 2020, **8**, 9039–9048.

8 W. Zhang, Y. Zhou, A. M. Hussain, D. Song, Y. Miura, Y. Chen, Z. Luo, N. Kane, Y. Niu, N. Dale, Y. Fukuyama and M. Liu, *ACS Appl. Mater. Interfaces*, 2021, **13**, 4993–4999.
9 H. Zhang, K. Xu, F. He, Y. Zhou, K. Sasaki, B. Zhao, Y. Choi, M. Liu and Y. Chen, *Advanced Energy Materials*, 2022, 2200761.
10 M. Bilal Hanif, M. Motola, S. qayyum, S. Rauf, A. khalid, C.-J. Li and C.-X. Li, *Chemical Engineering Journal*, 2022, **428**, 132603.
11 R. Hui, C. Sun, S. Yick, C. Decès-Petit, X. Zhang, R. Maric and D. Ghosh, *Electrochimica Acta*, 2010, **55**, 4772–4775.
12 C. Sun, J. A. Alonso and J. Bian, *Adv. Energy Mater.*, 2021, **11**, 2000459.
13 C. Sun, R. Hui and J. Roller, *J Solid State Electrochem*, 2010, **14**, 1125–1144.
14 P. A. Connor, X. Yue, C. D. Savaniu, R. Price, G. Triantafyllou, M. Cassidy, G. Kerherve, D. J. Payne, R. C. Maher, L. F. Cohen, R. I. Tomov, B. A. Glowacki, R. V. Kumar and J. T. S. Irvine, *Adv. Energy Mater.*, 2018, **8**, 1800120.
15 M. Li, K. Chen, B. Hua, J. Luo, W. D. A. Rickard, J. Li, J. T. S. Irvine and S. P. Jiang, *J. Mater. Chem. A*, 2016, **4**, 19019–19025.
16 Y. Tian, W. Wang, Y. Liu, A. Naden, M. Xu, S. Wu, B. Chi, J. Pu and J. T. S. Irvine, *ACS Catal.*, 2021, **11**, 3704–3714.
17 J. Cao, Y. Li, Y. Zheng, S. Wang, W. Zhang, X. Qin, G. Geng and B. Yu, *Advanced Energy Materials*, 2022, 2200899.
18 H. J. Choi, K. Bae, S. Grieshammer, G. D. Han, S. W. Park, J. W. Kim, D. Y. Jang, J. Koo, J.-W. Son, M. Martin and J. H. Shim, *Adv. Energy Mater.*, 2018, **8**, 1802506.
19 O. Celikbilek, C.-A. Thieu, F. Agnese, E. Calì, C. Lenser, N. H. Menzler, J.-W. Son, S. J. Skinner and E. Djurado, *J. Mater. Chem. A*, 2019, **7**, 25102–25111.
20 Z. Chen, L. Jiang, S. He, C. Guan, Y. Zou, Z. Yue, N. Ai, S. P. Jiang, Y. Shao and K. Chen, *Applied Catalysis B: Environmental*, 2022, **305**, 121056.
21 Y. Liu, Y. Tian, W. Wang, Y. Li, S. Chattopadhyay, B. Chi and J. Pu, *ACS Appl. Mater. Interfaces*, 2020, **12**, 57941–57949.
22 G. Li, Y. Gou, X. Cheng, Z. Bai, R. Ren, C. Xu, J. Qiao, W. Sun, Z. Wang and K. Sun, *ACS Appl. Mater. Interfaces*, 2021, **13**, 34282–34291.
23 H. Shimada, T. Yamaguchi, H. Kishimoto, H. Sumi, Y. Yamaguchi, K. Nomura and Y. Fujishiro, *Nat Commun*, 2019, **10**, 5432.
24 Z. Teng, Z. Xiao, G. Yang, L. Guo, X. Yang, R. Ran, W. Wang, W. Zhou and Z. Shao, *Materials Today Energy*, 2020, **17**, 100458.
25 T. Chen, Y. Zhou, M. Liu, C. Yuan, X. Ye, Z. Zhan and S. Wang, *Electrochemistry Communications*, 2015, **54**, 23–27.
26 H. Yu, H. Im and K. T. Lee, *Adv Funct Materials*, 2022, 2207725.
27 B.-H. Yun, K. J. Kim, D. W. Joh, M. S. Chae, J. J. Lee, D. Kim, S. Kang, D. Choi, S.-T. Hong and K. T. Lee, *J. Mater. Chem. A*, 2019, **7**, 20558–20566.
28 J. H. Park, C. H. Jung, K. J. Kim, D. Kim, H. R. Shin, J.-E. Hong and K. T. Lee, *ACS Appl. Mater. Interfaces*, 2021, **13**, 2496–2506.
29 J. Kim, S. Im, S. H. Oh, J. Y. Lee, K. J. Yoon, J.-W. Son, S. Yang, B.-K. Kim, J.-H. Lee, H.-W. Lee, J.-H. Lee and H.-I. Ji, *Sci. Adv.*, 2021, **7**, eabj8590.
30 J. Yan, Z. Zhao, L. Shang, D. Ou and M. Cheng, *Journal of Power Sources*, 2016, **319**, 124–130.

31 K. Joong Yoon, M. Biswas, H.-J. Kim, M. Park, J. Hong, H. Kim, J.-W. Son, J.-H. Lee, B.-K. Kim and H.-W. Lee, *Nano Energy*, 2017, **36**, 9–20.
32 Z. Shao, W. Zhou and Z. Zhu, *Progress in Materials Science*, 2012, **57**, 804–874.
33 M. Liu, M. E. Lynch, K. Blinn, F. M. Alamgir and Y. Choi, *Materials Today*, 2011, **14**, 534–546.
34 A. Hauch, R. Küngas, P. Blennow, A. B. Hansen, J. B. Hansen, B. V. Mathiesen and M. B. Mogensen, *Science*, 2020, **370**, eaba6118.
35 M. Singh, D. Zappa and E. Comini, *International Journal of Hydrogen Energy*, 2021, **46**, 27643–27674.
36 M. C. Offutt, *Department of Energy Funding for Hydrogen and Fuel Cell Technology Programs FY2022*, DOE, 2023.
37 K. Chen, N. Li, N. Ai, M. Li, Y. Cheng, W. D. A. Rickard, J. Li and S. P. Jiang, *J. Mater. Chem. A*, 2016, **4**, 17678–17685.
38 H. Liu, X. Zhu, M. Cheng, Y. Cong and W. Yang, *Chem. Commun.*, 2011, **47**, 2378–2380.
39 L. Zhang, D. Li and S. Zhang, *Ceramics International*, 2017, **43**, 2859–2863.
40 Y. Zhu, W. Zhou, Y. Chen and Z. Shao, *Angew. Chem. Int. Ed.*, 2016, **55**, 8988–8993.
41 Y. Chen, S. Yoo, Y. Choi, J. H. Kim, Y. Ding, K. Pei, R. Murphy, Y. Zhang, B. Zhao, W. Zhang, H. Chen, Y. Chen, W. Yuan, C. Yang and M. Liu, *Energy Environ. Sci.*, 2018, **11**, 2458–2466.
42 D. Ding, X. Li, S. Y. Lai, K. Gerdes and M. Liu, *Energy Environ. Sci.*, 2014, **7**, 552.
43 M. Choi, J. Paik, D. Kim, D. Woo, J. Lee, S. J. Kim, J. Lee and W. Lee, *Energy Environ. Sci.*, 2021, **14**, 6476–6483.
44 H. Abernathy, T. Yang, J. Liu and B. Na, 2021.
45 T. H. Wan, M. Saccoccio, C. Chen and F. Ciucci, *Electrochimica Acta*, 2015, **184**, 483–499.
46 Y. Chen, Y. Choi, S. Yoo, Y. Ding, R. Yan, K. Pei, C. Qu, L. Zhang, I. Chang, B. Zhao, Y. Zhang, H. Chen, Y. Chen, C. Yang, B. deGlee, R. Murphy, J. Liu and M. Liu, *Joule*, 2018, **2**, 938–949.
47 Y. Wang, T. Su, A. D. Brocato and X.-D. Zhou, *ECS Trans.*, 2019, **91**, 1527–1533.
48 H. Ren, Y. H. Lee, E. A. Wu, H. Chung, Y. S. Meng, E. E. Fullerton and N. Q. Minh, *ACS Appl. Energy Mater.*, 2020, **3**, 8135–8142.
49 Z. Jiang, Z. Lei, B. Ding, C. Xia, F. Zhao and F. Chen, *International Journal of Hydrogen Energy*, 2010, **35**, 8322–8330.
50 Y. Takeda, R. Kanno, M. Noda, Y. Tomida and O. Yamamoto, *J. Electrochem. Soc.*, 1987, **134**, 2656–2661.
51 D. A. Osinkin, *Electrochimica Acta*, 2021, **372**, 137858.
52 J. Hayd and E. Ivers-Tiffée, *J. Electrochem. Soc.*, 2013, **160**, F1197–F1206.
53 A. A. Kurteeva, S. M. Beresnev, D. A. Osinkin, B. L. Kuzin, G. K. Vdovin, V. D. Zhuravlev, N. M. Bogdanovich, D. I. Bronin, A. A. Pankratov and I. Yu. Yaroslavtsev, *Russ J Electrochem*, 2011, **47**, 1381–1388.
54 X. Xi, Z.-S. Cao, X.-Q. Shen, Y. Lu, J. Li, J.-L. Luo and X.-Z. Fu, *Journal of Power Sources*, 2020, **459**, 228071.

55 K.-Y. Lai and A. Manthiram, *Chem. Mater.*, 2018, **30**, 2515–2525.
56 O. Kwon, S. Sengodan, K. Kim, G. Kim, H. Y. Jeong, J. Shin, Y.-W. Ju, J. W. Han and G. Kim, *Nat Commun*, 2017, **8**, 15967.
57 C. Yang, J. Li, Y. Lin, J. Liu, F. Chen and M. Liu, *Nano Energy*, 2015, **11**, 704–710.
58 S. Sengodan, S. Choi, A. Jun, T. H. Shin, Y.-W. Ju, H. Y. Jeong, J. Shin, J. T. S. Irvine and G. Kim, *Nature Mater*, 2015, **14**, 205–209.
59 Z. Wang, Z. Wang, W. Yang, R. Peng and Y. Lu, *Journal of Power Sources*, 2014, **255**, 404–409.
60 L. Yang, Y. Choi, W. Qin, H. Chen, K. Blinn, M. Liu, P. Liu, J. Bai, T. A. Tyson and M. Liu, *Nat Commun*, 2011, **2**, 357.
61 Z. Zhan and S. Barnett, *Solid State Ionics*, 2005, **176**, 871–879.
62 Y. Tian, J. Li, Y. Liu, J. Yang, B. Liu, L. Jia, J. Jiang, B. Chi, J. Pu and J. Li, *International Journal of Hydrogen Energy*, 2018, **43**, 12603–12609.